Distribution and dynamics of water in the blended pastes unraveled by thermoporometry and dielectric properties

N.B. When citing this work, cite the original published paper.

(article starts on next page)

Distribution and dynamics of water in the blended pastes unraveled by thermoporometry and dielectric properties

Liming Huang [a,b,*], Helén Jansson [a], Jan Swenson [c], Luping Tang [a], Zhenghong Yang [b]

[a] *Department of Architecture and Civil Engineering, Chalmers University of Technology, 41296 Gothenburg, Sweden*
[b] *Key Laboratory of Advanced Civil Engineering Materials Ministry of Education, Tongji University, Shanghai 201804, PR China*
[c] *Department of Physics, Chalmers University of Technology, 41296 Gothenburg, Sweden*

ABSTRACT

Water distribution in hardened paste and its dynamics determine many properties related to durability. Moisture distribution was determined by thermoporometry combined with vacuum drying. Dynamics of confined water were measured by broadband dielectric spectroscopy. Water in pores <2.4 nm cannot form tetrahedral ice structure due to geometrical constraints. The volume of unfrozen water (in interlayer and gel pores) decreases after the drying at all relative humidity levels. An evident coarsening of gel pores occurs with drying between 75 % and 55 % RH. 35 % fly ash and slag have limited effects on relaxation processes of silanol hydroxyl groups and interlayer water. However, they slow down the dynamics of water in small gel pores, thereby enhancing interactions between water and the solid interface. This study clarifies the microstructural changes during the drying and reveals the sensitivity of water dynamics to the chemical environment in C-S-H of blended pastes.

1. Introduction

Water, one of the main ingredients for concrete production, is greatly involved in the reaction of cementitious materials. It has the function of a "carrier" to dissolve ions from mineral surfaces to form a solution, and then builds itself into the chemical structure of hydration products. Furthermore, it also plays a critical role in determining deterioration of cement-based materials by controlling transport properties [1,2] and corrosion reactions [3]. In addition, freeze-thaw induced damages [4,5] and alkali-silica reaction [6] are rather sensitive to the water confined in the porous matrix. Therefore, it is of great interest, both from scientific and practical perspectives, to have a clear understanding of the moisture distribution in the porous structure at different relative humidity (RH) conditions and how this affects dynamics of water confined in nanopores of cement-based materials.

Supplementary cementitious materials (SCMs) are widely used in cement-based materials to reach the goal of reducing CO_2 emissions from the construction sector [7,8]. Incorporation of SCMs impacts the microstructure of hardened cement-based materials (hcp). Our previous investigation identified the effects of typical SCMs (fly ash, slag and limestone) on nanopore structure by water vapour desorption isotherms [9]. However, the sorption isotherm demonstrates the total moisture

content in pores smaller than a critical value, and it cannot be used to characterize the detailed distribution of water in hcp at a specific relative humidity. Low-field nuclear magnetic resonance is widely used as a nondestructive method to quantify the spatial distribution of water in porous materials and to characterize the microstructure of calcium silicate hydrate (C-S-H) [10–13], but the application of this technique is limited for white cement and some other selected materials. Because the presence of paramagnetic elements (such as Fe and Mn) increases the surface relaxation of water [14], which will interfere the quantitative description of geometry effects, it can hardly be used in detecting the pore size distribution of pastes with Portland cement and typical SCMs.

One alternative method to detect the water distribution under geometrical confinement is low-temperature differential scanning calorimetry (LT-DSC). Brun et al. [15] proposed a method, defined as thermoporometry, to calculate the size of pores filled with a liquid by studying the thermodynamics of liquid-solid phase transformations in porous materials. Provided a nearly saturated condition, thermoporometry was well applied to investigate the pore size distribution of hydrated calcium sulfoaluminate cement pastes [16,17] and Portland cement mortar [18]. However, it has been found that the extremely confined water can avoid crystallization at any temperature, given that the pore size (width < ~2 nm) is too small for water molecules to form a

---

tetrahedral ice structure [19]. The interlayer space and small gel pores in C-S-H present this kind of restriction. Water in such parts helps to understand the structure of C-S-H [11,20] and corresponds to the irreversible shrinkage [21]. A recent study named the interlayer space (<1.4 nm) as rigid gel pores because their size and volume had few changes during the first drying and wetting [22]. The moisture distribution in hcp under different RH levels is a complex problem since the volume of nanosized pores show dynamical changes during the drying process. There was a debate about whether the volume of gel pores would be largely increased by drying under 85 % RH [23,24], in which the different criteria for classification of gel pores also elevated the contradiction in understanding the dynamic process. The concept of gel pores in hcp was originally proposed by T.C. Powers and T.L. Brownyard [25]. They classified the pores with the width < 2.7 nm as gel pores, which part of the pores is inside the gel-like products and is rather stable due to the size being smaller than the limitation of hydration products nucleation. H.M. Jennings [26,27] assigned the pores from 1 nm to 12 nm as gel pores based on a colloidal model of C-S-H. Different classifications were also proposed according to dynamics of water tested by proton nuclear magnetic resonance, with values varying between 1.5 nm and 5 nm [11,20,28]. LT-DSC test may be useful to resolve some part of the puzzle about how moisture redistributes in gel pores during the drying and improves the understanding of the C-S-H structure.

The behavior of water in hcp at low temperatures, practically, determines the potential frost damage of cement-based materials. The phase transition of freezable water to ice induce hydraulic pressure by expelling the unfrozen water [29]. Moreover, a continuous cooling causes the cryo-suction process that drives the liquid towards the frozen sites [30]. These water migration processes are closely related to the distribution of freezable and unfrozen water in the porous matrix as well as the dynamics of water confined in the nanosized pores. Confined water has distinguishing structure and dynamical properties that differs from bulk water [19,31,32]. Broadband dielectric spectroscopy (BDS) has been widely used in the investigation of water dynamics confined in C-S-H at various temperatures. However, the understanding of the dynamical behavior and the local confining environment of water in C-S-H are different in several papers. Cerveny et al. reported [33] three relaxation processes of water in C-S-H gel that were assigned to be chemical bound water, water in small pore <1 nm and large gel pore water, respectively. Garcia-Lodeiro et al. [34] also detected three relaxation processes but their interpretations of the three processes are somewhat different. Goracci et al. [35] found four relaxation processes, each one corresponding to different confining conditions, and they assigned processes 3 and 4 to water in small gel pores and large gel pores, respectively, by referring to Jennings's colloidal model [27]. A comparison between the relaxations in synthetic tobermorite and xonotlite provided a more detailed description of the fastest relaxation processes of water in C-S-H systems [36]. Overall, there is a lack of a general and comprehensive understanding of water dynamics in hcp, and it is short of investigations of how SCMs influence the distribution and dynamics of water.

This study used LT-DSC to quantitatively describe the distribution of water confined in different pores after drying at various equilibrium conditions. Insights will be provided for the distribution of water in capillary pores and gel pores in relation to freezable and unfrozen (supercooled) water. BDS was used to investigate the dynamics of water confined in the hcp. Different relaxation processes will be analyzed in correspondence to local chemical environments of the C-S-H microstructure, and this study will provide a comprehensive understanding of how the water dynamics are affected by the local environment. The effect of SCMs on the distribution of water confined in pores, as well as the dynamics of water, is elucidated for understanding how the microstructure in the blended pastes and the drying process affect water dynamics.

2. Materials and methods

2.1. Preparation of samples

Detailed information of materials and mixing procedure has been illustrated in a previous publication [2]. Table 1 shows the binder mix of samples in this paper. Portland cement (CEM I 52.5 R) was used as reference (noted as P045). Binary systems were made by replacing cement with 35 % siliceous fly ash (P145) and 35 % slag (P245), respectively. In the ternary system (P345), cement was replaced by 35 % slag and 16 % limestone. All the binder systems were mixed with a water to binder ratio of 0.45. After one week of sealed curing, the samples were crushed into particles smaller than 1 μm and then water cured for two months. Afterwards, particles were moved into conditioning boxes with four different RH levels (97.6 %, 75.5 %, 54.4 % and 33 %) controlled by saturated salt solutions at 20 °C [37]. Portlandite was put on the top layer of each conditioning box as absorbent of CO_2 to avoid carbonation of pastes. All the measurements were operated for samples after 1.5 years of conditioning. The total evaporable water content in the hardened pastes was measured by vacuum drying of particles at 25 °C for 1 week.

2.2. Low temperature differential scanning calorimetry

LT-DSC measurements of powder samples were performed using the TA instrument DSC Q2000. Samples with a weight of about 20 mg were put in hermetical sealed aluminum pans. The samples were firstly cooled from 20 °C to −60 °C with a rate of 2 °C/min, and then equilibrated for 5 min before reheated to 20 °C with the same rate. Samples conditioned at 97 % RH were measured with a second cycle using the same protocol. To better compare the signals of the different binder systems, a normalization was done to obtain a similar starting point of all curves. To reach a similar ion concentration as pore solution of samples, a mimic pore solution was made by adding 150 mmol/L KCl and 50 mmol/L NaCl into the extracted pore solution of CEM I paste with a water-binder-ratio of 1. It was then measured with the same cooling procedure for evaluating the heat from fusion of the pore water in hcp.

2.3. Broadband dielectric spectroscopy

The well-conditioned particles were ground to a powder prior to testing. The complex dielectric permittivity of the powder samples was measured by a broadband dielectric spectrometer (Novocontrol Alpha-N) in the frequency range 10^{-2}-10^{6} Hz. Isothermal frequency scans were performed at temperatures from −147.15 °C to 26.85 °C (130−300 K) with an increment of 5 °C (K). The sample temperature was controlled with a deviation lower then ±0.1 K. Parallel gold-plated electrodes with a diameter of 10 mm were used to tightly hold the powder samples (about 0.5 g). The thickness of each sample was ~0.2 mm.

3. Results and discussion

3.1. Thermoporometry analysis of LT-DSC

According to the thermodynamic properties of water-ice phase transformation, the relationship between pore size and solidification temperature can be estimated by the Gibbs-Thomson equation [15,18].

Table 1
Binder mix of each sample.

Sample name	P045	P145	P245	P345
Mix by weight	100 % CEM I	65 % CEM I + 35 % fly ash	65 % CEM I + 35 % slag	49 % CEM I + 35 % slag+16 % limestone

$$r_p = \frac{A}{\Delta T_s} + \delta \tag{1}$$

where r_p (nm) is the radius of the cylinder pore, ΔT_s (°C) is undercooling temperature compared to the melting point of bulk ice crystals, A is a constant determined by the surface energy between water and cement-based material, and δ is a constant related to the layer thickness of unfrozen water and the pore shape. The shape of the pores is normally assumed to be cylindrical. Parameters A and δ have been taken as 64.67 and 0.57 for the freezing process, and 32.33 and 0.69 for the melting process [18].

Based on a comprehensive consideration of the baseline for LT-DSC and the difference in the heat capacity of the different phases (liquid, ice crystals and porous body), the amount of ice formation at different temperatures can be calculated by Eq. (2) [18].

$$m_c(T + n\Delta T) = m_c(T) + \sum_1^n \frac{\Delta T}{2} \left[\frac{Q(T + n\Delta T - \Delta T) - Q_0}{qh_f} + \frac{Q(T + n\Delta T) - Q_0}{qh_f} \right] exp\left[\frac{\Delta T(C_{pC} - C_{pL})}{h_f} \right] \tag{2}$$

where $m_c(T)$ is the ice mass at temperature T with respect to the original sample weight, ΔT is the temperature interval (selected to be 0.02 °C in this study), h_f (J/g) is the heat of fusion for pore water, $Q(T)$ (W/g) is the heat flow into samples, Q_0 (W/g) is the heat flow of baseline, q (°C/s) is the heating rate, C_{pL} (J/g/°C) is the heat capacity of the pore liquid and C_{pC} (J/g/) is the heat capacity of ice crystals. The fusion heat of the pore solution was obtained by measuring the DSC curve of the mimic pore solution, as described in Section 2.2. The heat capacity of the pore liquid and the ice as a function of temperature is described by Eqs. (3) and (4), respectively. The temperature dependence of ice density (ρ_i) is given by Eq. (5) [15].

$$C_{pC} = 2.114\left(1 + 3.737 \times 10^{-3}T\right) \tag{3}$$

$$C_{pL} = 4.222\left(1 - 5.4 \times 10^{-4}T\right) \tag{4}$$

$$\rho_i \approx 0.9167 - 2.053 \times 10^{-4}T - 1.357 \times 10^{-6}T^2 \tag{5}$$

As shown in Fig. 1a, the baseline of LT-DSC, on cooling, is described by a straight line from the freezing start to about −55 °C. The baseline of the heating curve is horizontal and normalized to be about 0 W/g. A significant hysteresis can be observed in the freezing-melting curve of hcp. The average melting temperature is considerably higher than the average freezing temperature, which is in agreement with the freezing and melting of water in many other porous media [38]. This is mainly because of a geometrical hindrance effect from the pore shape, making crystallization more difficult than bulk water. The attractive potential from the pore walls also induces a compression effect, so the competition between the hindrance and compression results in a non-monotonic correlation between the freezing temperature and the pore diameter [39]. An extreme confinement (pore diameters less than about 2 nm) will even inhibit the water molecules from forming ice crystals [19]. Sun and Scherer [18] concluded that there was no freezing in pores with a width smaller than 4.5 nm. Bager and Sellevold [40] reported that no ice was formed in hardened cement paste equilibrated at RH of 33 % and 11 %. No exothermic peak was detected in white cement paste at 33 % RH [41] as well. Fig. 1b shows no indication on crystallization of water in P045 and P145 at RH of 33 %, but crystallization is detected in the slag blended pastes (P245 and P345) equilibrated at the same RH. This interesting result may be induced by the refined ink-bottle shape of pores with small necks [9]. During the drying process, it is difficult to dry the inner parts of these pores. It may also be due to the expelling of

water from interlayer or small nanosized pores to larger pores during the cooling process, which is similar to the freezing process of montmorillonite [42]. Further experiments are needed for an in-deep understanding of this phenomenon.

Fig. 2a shows the distribution of ice volume in cement paste under different RH levels, calculated by Eq. (2). Due to low crystallization degree in hcp in equilibrium with 33 % RH, the curves of samples with this RH are not presented. As expected, the volume of ice in hcp decreases as it is dried at lower RH levels. The hysteresis of the freezing and melting process is observed under all RH conditions. After the calculation of the cylinder pore width with Eq. (1), the cumulative freezable water distribution with respect to pore size can be obtained as shown in Fig. 2b. The hysteresis in freezing and melting data is more evident based on the difference in the lowest pore width for the formation of ice crystal. The freezing curves seem to imply that the critical pore width is about 4 nm, so it means that there is no ice formation in pores smaller than this value. However, the crystallization peak was detected in silica nanopores with diameters of 3 nm [43]. Molecule dynamics modelling also indicated that the critical size for the nucleation of ice is with a gyration radii of 1 nm [44]. The pore size based on the melting curve has
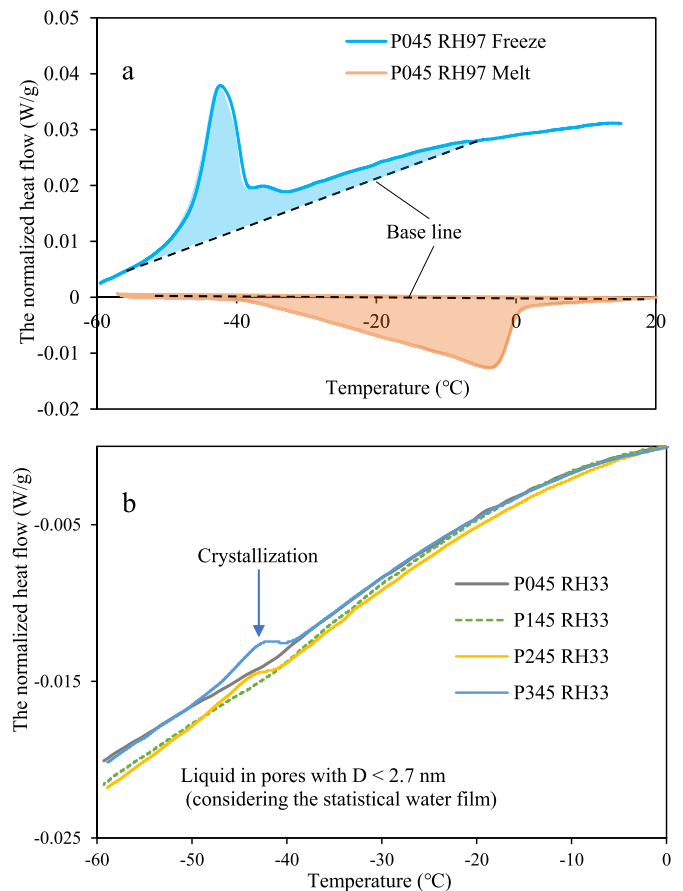

Fig. 1. Typical LT-DSC curves of cement-based materials, exemplifying with CEM I paste conditioned under RH of 97 % (a) and pastes conditioned under RH of 33 % (b). In (a), the upper curve shows the results of cooling and the lower the heating curve. In (b), the results of cooling.
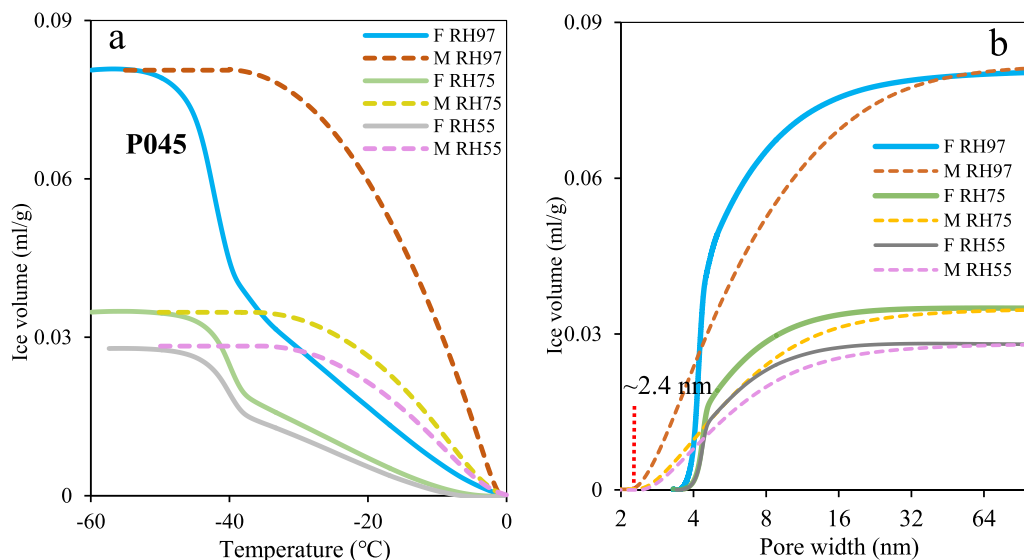
Fig. 2. The calculated ice volume in P045 conditioned with RH of 97 %, 75 % and 55 % using Eq. (2) (a) and the corresponding ice volume in nanopores based on Eq. (1) (b) with respect to freezing (noted as F) and melting (noted as M) process.
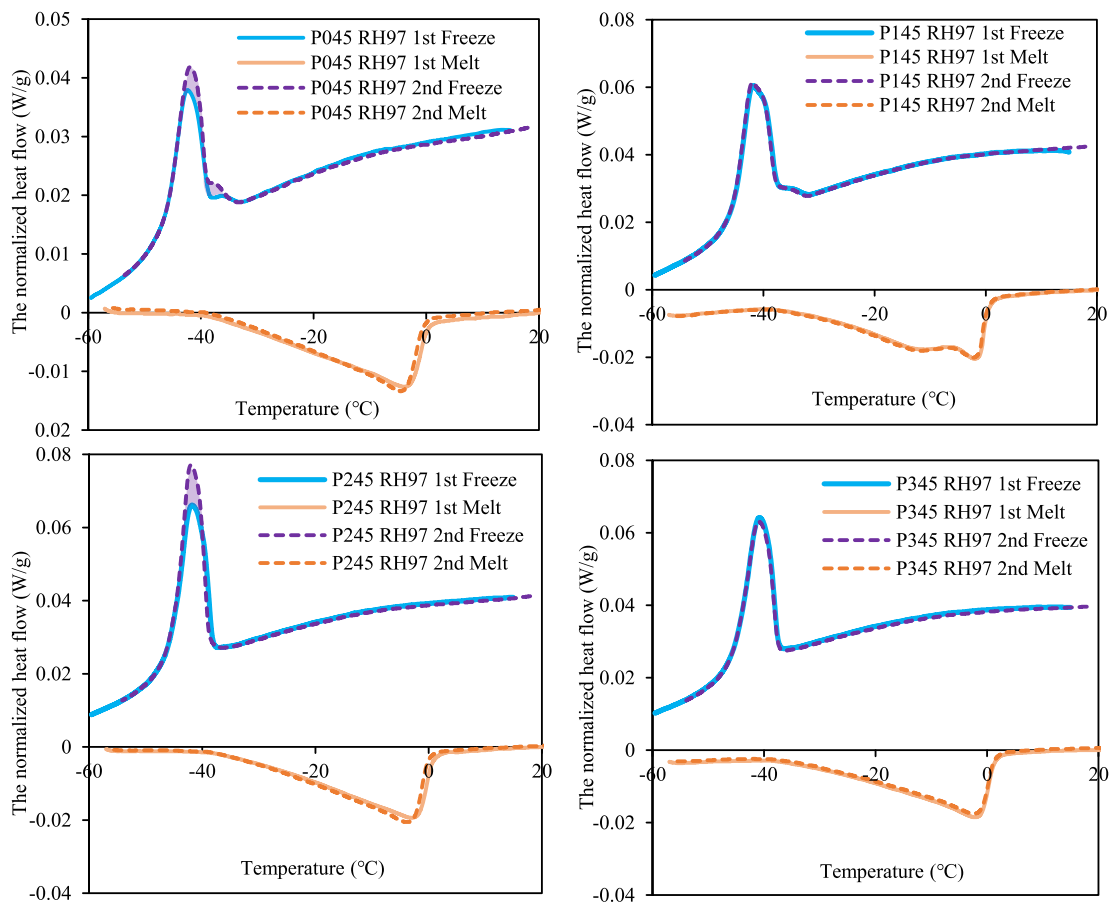

Fig. 3. Effect of cyclic freezing and melting experience on the DSC curves of hcp.

a critical diameter of 2.4 nm, so it is obvious that melting curves are more reasonable for evaluation of the water distribution in hcp. The hysteresis becomes weaker in hcp conditioned at lower RH levels.

An exposure of cement-based materials to low temperatures will change the microstructure of the matrix [45], which impacts the mechanical performance [5]. To assess the effect of LT-DSC measurement on the distribution of water, a second freezing-melting scan was performed immediately after the first. Fig. 3 shows that the second LT-DSC scan is almost identical to the first test for P145 and P345, indicating a reversible behavior of the water transport during the cooling process. However, the first freezing-thawing cycle induces an increase in the freezable water content in P045 and P245, as clearly seen from the

increase of the crystallization enthalpy in the second scan. This is probably due to the expelling of interlayer water into gel pores during the freezing. P045 and P245 have a higher C-S-H content than the other two samples in a well-hydrated condition [9]. Moreover, incorporation of *Al* in the C-S-H structure will stabilize the layer structure [46] to mitigate the effect of drying as well as freezing. The combination of these effects causes the difference in the moisture redistribution in hcps under the freeze-thaw process. However, for P045 and P245 the LT-DSC results show that there are generally only weak irreversible effects on the moisture distribution.

3.2. Effect of SCMs on the moisture distribution during the first drying

Supplementary cementitious materials impact the phase assemblage

of hydration products, change the size and total volume of pores, and influence the durability of cement-based materials [47]. The distribution of freezable water can be calculated by taking the derivative of the cumulative ice volume with respect to the pore width. Fig. 4 presents a comparison of the ice formation in the different binder systems, based on both freezing and melting curves. The distribution of freezable water in the pores is significant since it determines the frost performance of the cement-based materials [5,48,49]. During the drying process, water confined in pores of different sizes would also influence the diffusion of moisture [2] and the shrinkage in hcp [50].

Compared to the pore size distribution calculated using water vapour sorption data, Fig. 4 presents the clearer information about the distribution of moisture at each RH. The fly ash blended paste has the highest ice content at 97 % RH. Most of the differences are detected for the water
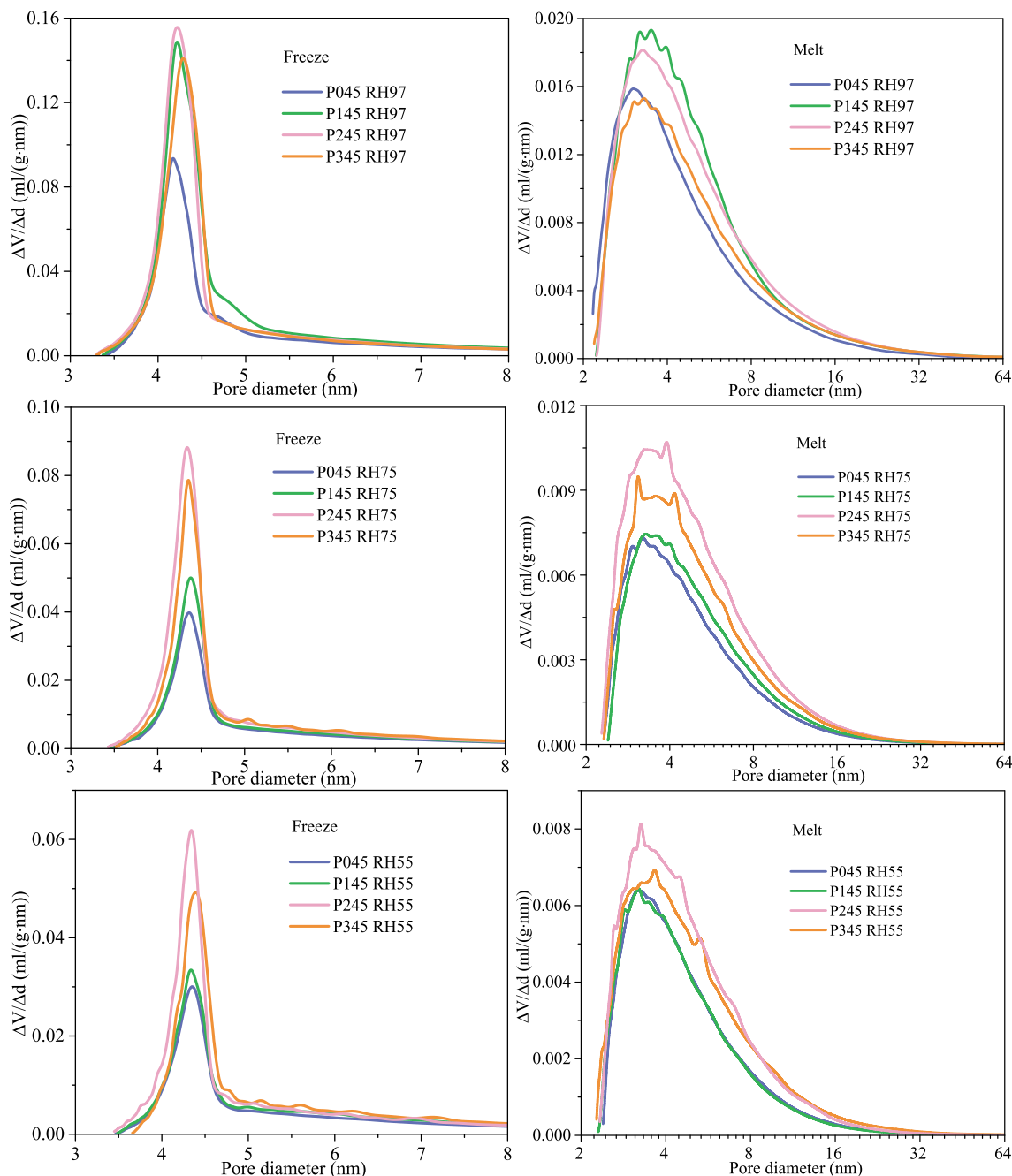

Fig. 4. Comparison of the calculated ice distribution with respect to pore size in samples conditioned at RH of 97 %, 75 % and 55 %. The distributions are obtained from both the freezing (left panels) and melting (right panels) heat curve.

confined in pore sizes from 4 nm to about 8 nm, which can be observed in both the freezing and melting curves. The melting curves show that the slag binary paste seems to have lower content of water in pores from 3 nm to 8 nm, but a higher water content in pores larger than 8 nm, compared to the fly ash blended paste. The CEM I paste has the lowest ice formation in all ranges of pores. These findings are somehow consistent with the measured moisture content by water vapour isotherms [9] and the pore size distribution in the same mixes with different curing conditions [2]. A further replacement of CEM I with limestone reduces the freezable water content compared with the binary slag paste.

The initial ice formation temperature of paste at 97 % RH is lower than that temperature of paste at 75 %, and a drying from 97 % to 75 % RH results in a clear reduction in the volume of ice in pastes. This phenomenon was observed not only in cement-based materials [40] but also for water in porous silica media [43]. Fly ash blended paste has a much lower content of ice than the slag blended pastes at 75 % RH. This implies that a large part of the freezable water is dried in the fly ash paste from 97 % to 75 % RH, resulting in the fly ash blended paste having a similar amount of ice as the CEM I paste. Several publications reported that an appropriate amount of fly ash mixed into concrete can effectively

improve the freeze-thaw resistance [48,51]. The freeze-thaw performance is actually related to the volume of freezable water in hcp, so the saturation condition is a critical factor for a given mix [49]. Therefore, it is important to consider the saturation conditions in correspondence to service environment when investigating the effect of fly ash or slag [52,53] on freeze-thaw properties. When exposed to a moderate water-saturation environment (such as XF1 and XF2 in EN 206–1), the paste with 35 % fly ash may have the best freeze-thaw resistance at a RH of 75 % due to its low amount of freezable water and high amount of air-filled pore volume. While exposed to a high water-saturation environment (such as XF3 and XF4 in EN 206–1), it may have the worst frost resistance due to its high volume of freezable water at 97 % RH.

At RH of 55 %, the distribution of freezable water in the fly ash blended paste is almost the same as that of the CEM I paste. At the same RH, slag blended pastes have formed a much higher amount of ice than the other two binder systems. This can be explained by the effect of slag on the pore structure, which increases the volume of pores in range from 4 to 10 nm (noted as gel pores in [54]). The observed redistribution of moisture is mainly caused by the drying process but also mixed with some effect from water transport during the freezing and thawing process. However, it is apparent that the drying process is not just emptying
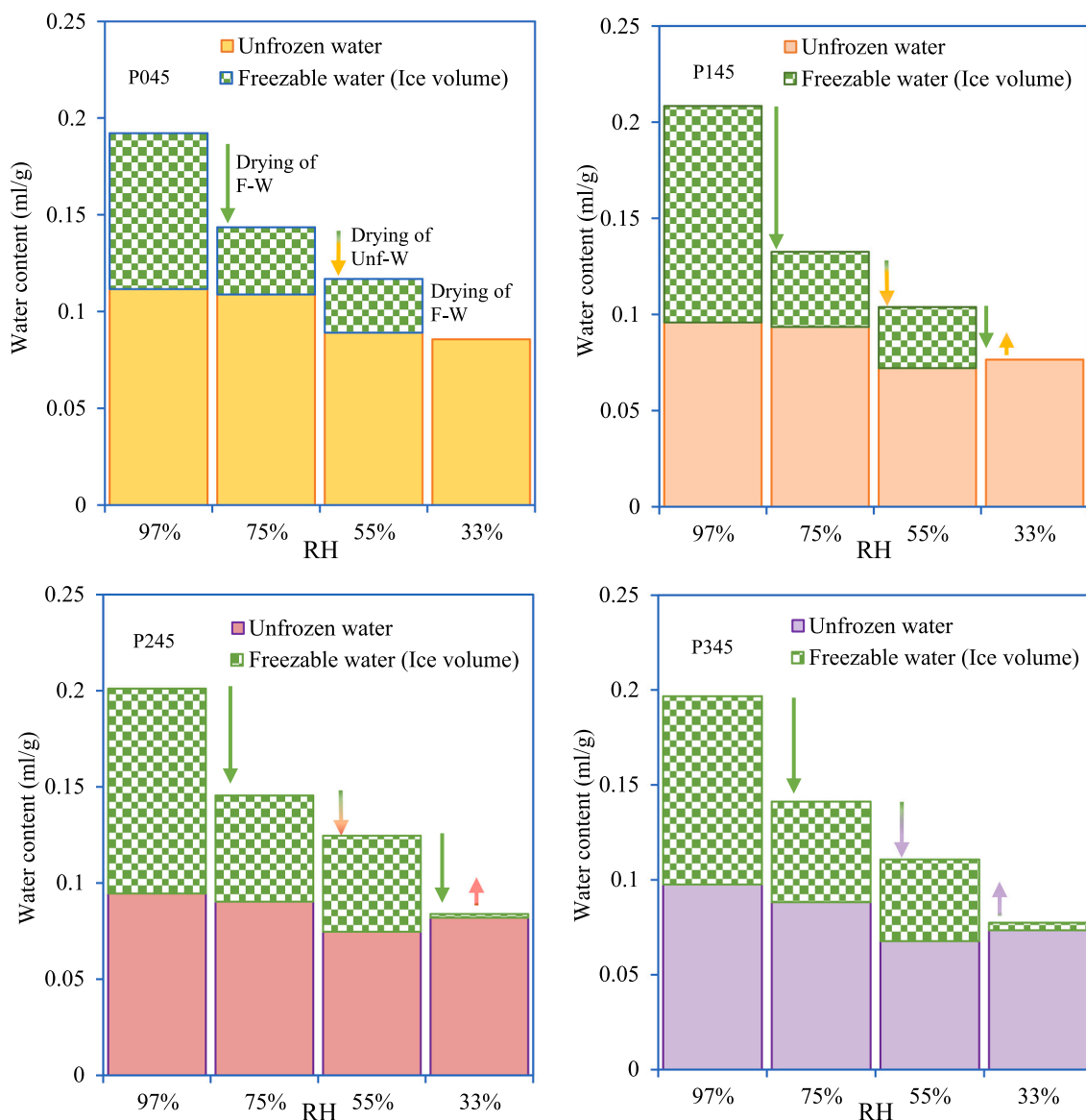

Fig. 5. Moisture distribution in hcps during the desorption process indicated by the reduction in freezable water (F—W) and unfrozen water (Unf—W).

water from larger to smaller pores. Rather, water in all size ranges of pores is affected by drying, and this will be detailed in next section.

3.3. Distribution of water under different RH levels

Drying of cement-based materials causes microstructural change of the main hydration products, such as contraction of layer and coarsening of capillary pores [9,55,56]. This dynamical change of the structure may induce an anomalous evolution of moisture redistribution, thereby increasing the portion of water in small pores while drying the large pores [57]. Fig. 5 demonstrates the content of freezable and unfrozen (supercooled) water in the cement-based pastes at different RH levels after the first drying process. Water in pores with a diameter smaller than 2.4–2.7 nm cannot form ice crystals [19,43,44,58], so water in such confinements is not giving rise to any crystallization or melting peaks in the LT-DSC curves. This unfrozen part of the water was calculated by subtracting the volume of freezable water from the total evaporable water content measured by the vacuum drying.

Compared with samples at a RH of 97 %, drying to 75 % RH mainly decreases the freezable water content in hcp. The unfrozen water content shows a minor decrease, which keeps almost constant in P045, P145 and P245. Referring to the definition by H.M. Jennings [27], the water in interlayer and small gel pores (SGP) show few changes, and the main drying occurs in large gel pores and capillary pores. However, the criteria for classification of gel pores vary in different references as shown in Table 2. According to T.C. Powers and T.L. Brownyard [25], the unfrozen water is exactly the water in gel pores, whereas in classification based on other publications it includes both water in interlayer space and gel pores [11,20,28,57,59]. It has been under a heated discussion about whether the drying of cement-based materials induces an increase in the content of "interlayer water" at a RH of ~80 % [23,24,57]. The "interlayer water" in the previously discussed papers is based on proton NMR relaxation measurements, and referred to water in pores < ~3 nm [13,20]. This part of the water accounts for most of the evaporable water in hcp at a RH of 80 %. It is an extreme confinement condition, and therefore it is expected to be of the same amount as the unfrozen water. According to the distribution of unfrozen water, the drying at a RH of 75 % presents no increase in volume of water under such a confinement in both CEM I and the blended pastes.

It is interesting that the hcp dried at a RH of 55 % has a much lower content of unfrozen water than those dried at a RH of 75 %. It seems that the amount of freezable water shows a very small reductions from 75 % to 55 % RH, especially in the blended pastes. A drying down to 55 % RH causes a contraction of the layer distance in C-S-H [57,60,61], and decreases the statistical thickness of the surface water layer [9]. Moreover, the water removal process induces the movement of some C-S-H sheets, which results in a coarsening of gel pores [23,56,62]. Together, these effects give rise to that the volume of freezable water at 55 % RH is similar to that at 75 %. This result implies that the coarsening of gel pores evidently occurs during the drying within this RH interval. The cooling process may also cause the migration of unfrozen water into freezable pores, which can induce a screening effect on water redistribution caused by the microstructural change. Provided that pores in hcp show no dynamical changes, the drying at 75 % and 55 % RH

Table 2
Summary of the criteria for classification of gel pores in representing publications.

References	Assigned interval for gel pores
T.C. Powers and T.L. Brownyard [25]	<2.7 nm
I. O. Yaman et al. [59]	0.5 to 4 nm
H.M. Jennings [27]	1 to 3 nm (SGP) and 3 to 12 nm (LGP)
P.J. McDonald et al. [28]	1.5 to 4.1 nm
A.C.A. Muller et al. [13,20]	3 to 5 nm
A. Valori et al. [11]	2 to 5 nm
Ippei Maruyama et al. [24]	1.87 to 3.4 nm, ~5.35 ± 0.63 nm

corresponds to empty open pores with a diameter larger than ~8 nm and ~ 4 nm, respectively, according to the Kelvin equation, H.M. Jennings et al. [63] hypothesized that water in this range is closely related to the structure of low-density C-S-H, and the rearrangements of microstructure within this RH range was associated with irreversible shrinkage [64,65]. Therefore, the redistribution of this part of water is significant to understand the correlation between microstructure change of C-S-H and properties of cement-based materials. An equilibrium at 33 % RH dries out vast majority of the freezable water, but it causes a slight increase in the amount of unfrozen water in the blended hcp compared with the hcp at a RH of 55 %. This can be ascribed to the transformation of some gel pores into the interlayer spaces [57]. Drying at 33 % RH may also induce the piling of C-S-H [66] to form more surface area for absorbing unfrozen water.

Fig. 6 illustrates the detailed distribution of evaporable water in hcp during the first drying. The water distribution has been classified into four intervals: <2.7 nm, 2.7–10 nm, 10–20 nm and >20 nm, and the amounts of evaporable water in these ranges were obtained by combining data of the melting curve in Fig. 4 with the amount of unfrozen water in Fig. 5. The data of P045 and P145 show that the amount of water confined in interlayer and gel pores change during the drying at any RH condition. It is again confirmed that the water in interlayer and small gel pores (<2.7 nm) never shows an increase during the first drying process under equilibrium. Water in capillary pores is almost completely dried out at 75 % RH. In addition, there is a loss of more than half of the water in large gel pores (2.7–10 nm) [27], also named interhydrate spaces [13,20]. At RH of 55 %, only a small fraction of the water constraint within these pores is lost, in contrast to a drying at RH of 75 %, and the main loss is detected for water in the interlayer and small gel pores (<2.7 nm). A drying at 33 % RH completely removes the water in large gel pores (>2.7 nm). A minor increase in the amount of unfrozen water can be understood as a result of C-S-H sheets movement mixed with some effect of water transport during freezing.

3.4. Dynamics of the confined water in hardened paste

Electric polarizability of water in nanosized regions relates to the local chemical environment, which determines the strength of water-mediated intermolecular forces. It affects various properties of a material, such as surface hydration, ion solvation, molecular transport in nanopores and chemical reactions [67,68]. The frequency-dependent dielectric response of water in hcp is influenced by the confinement condition as well as the temperature of the material [33,69,70]. A spatial confinement on a nanoscale alters the molecular dynamics of water by affecting dipolar rotations and reorientations. Fig. 7 shows how the dielectric permittivity depends on the frequency and temperature in a BDS measurement. Five relaxation processes (R1 to R5) can be detected for hcp at a RH of 97 %.

Because the dielectric processes show a symmetric feature with respect to frequency, the Cole-Cole function [71] has been used to fit the imaginary part of the dielectric permittivity at the different temperatures, as shown in Eq. (7).

$$\varepsilon^* = \varepsilon_\infty + \frac{\Delta\varepsilon}{1 + (i\omega\tau)^\alpha} \tag{7}$$

where $0 < \alpha \leq 1$ leads to a symmetrical broadening for the relaxation function, compared to a Debye relaxation (which corresponds to a single exponential relaxation in time domain). $\Delta\varepsilon$ is the relaxation strength, and ε_∞ is the dielectric constant at "infinite frequency". ω is the angular frequency, ε^* is the complex dielectric permittivity, and τ is the generalized relaxation time.

As an example, Fig. 8a presents the fitting results of the P045 sample at three selected temperatures. Fig. 8b to d demonstrate the temperature dependence of the relaxation time, broadening parameter, and relaxation strength of each relaxation process. The relaxation process 1 (R1) is
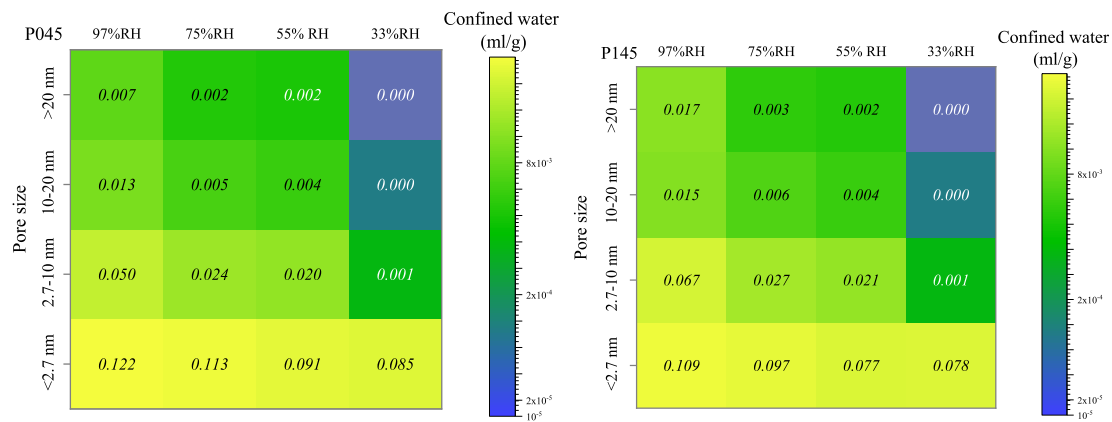
Fig. 6. Detailed moisture redistribution in hcp during the first drying process, exemplified by P045 (left) and P145 (right).
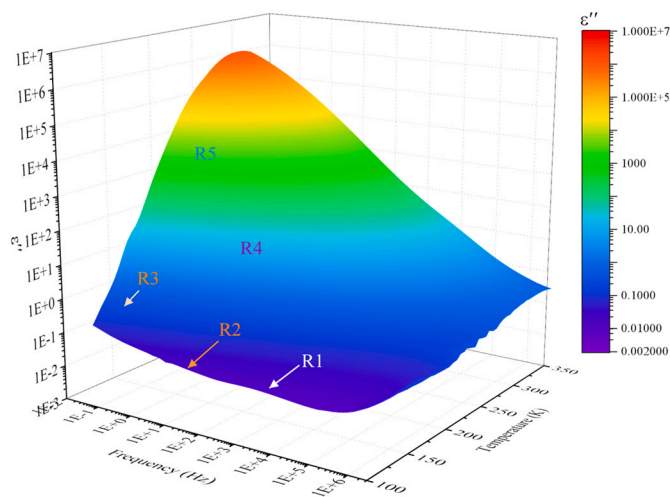

Fig. 7. Typical three-dimensional temperature and frequency dependences of the dielectric permittivity ε'' of hcp heated from 130 K to 350 K (exemplified by P045).

fastest and has the lowest activation energy. This process was found even in C-S-H dried at 120 °C [33], and it was hypothesized to arise from rotation or reorientation of hydroxyl groups bound to the structure. Musumeci et al. [36] performed a comparative study of the synthetic xonotlite and tobermorite to distinguish the dynamics of Ca-OH and Si-OH environments, and showed that hydroxyl groups bound to the Ca atom have a faster dynamics and lower activation energy then those bound to Si. According to this, the R1 process in Fig. 8b has the characteristics of hydroxyl in Si-OH environment. The broadening parameter of R1 stays almost constant from 130 to 170 K, while its relaxation strength shows a minor increase after 150 K.

Relaxation process 2 (R2) was also reported in many previous investigations of water confined in synthetic C-S-H and Portland cement pastes [33,35,36,72]. It is the second fastest process and which is caused by the strong local interactions of water with surface groups and charge compensating cations. The local chemical environment of water molecules consists of solvation/hydration water close to the hydroxyl groups and near the charge compensating cations (Ca^{2+} or Na^+). Vasilyeva et al. [73] claimed that this process was not observed in glass materials, so it was assumed that R2 reflected the water molecules near hydrated cations located in the interlayer of clay materials. However, this process has been found in silica matrices MCM-41 [74,75] and in the synthetic tobermorite [36] where there are no interlayer cations existing. Therefore, a more reasonable interpretation is that R2 process is the dynamics of water molecules hydrating the silanol groups [76] or water confined

in small pores <1 nm [33]. This process is very sensitive to the local environment, which means that the presence of different cations will impact its dynamics.

Relaxation process 3 (R3) has a broadening parameter of about 0.5, and its relaxation strength ranges from 0.5 to 4 (see the values for other samples in the Supplementary Information, SI). This process is considered to be an "universal" relaxation process of the confined water, as it is present in all kinds of confinements [19]. In fact, it is even present in amorphous bulk ice (or supercooled bulk water) [77], which indicates that it is an intrinsic local relaxation of water molecules and not substantially affected by interactions with surfaces or types of molecules or ions. However, this relaxation process will be affected by a reduction in the number of hydrogen bonds between the water molecules, particularly in the case of hydrophilic host materials [78]. Water confined in pores from 1 to about 2.4 nm is inhibited to form a network structure of tetrahedrons by building four hydrogen bonds for each molecule, but these molecules may form small clusters connected by more than one hydrogen bond [33]. Fig. 9 presents a comparison of the dynamics of water in fly ash blended paste (P145) in equilibrium at 97 % and 33 % RH, together with data of bulk ice relaxation from Refs. [79, 80] for comparison and a better understanding of the different types of water in hcp. R3 in hcp is close to the dynamics of ice in tri-propylene glycol solution [80]. At low temperatures, the ice is also occupying a large volume of the pores in hcp at a RH of 97 %, so R3 may also include the relaxation of crystalline ice. However, it is not only due to the relaxation of ice as it is also observed in the hcp at the RH of 33 %, in which there is almost no ice crystallization, as measured by LT-DSC (see Fig. 1 and Fig. 5). R3 in P145 at the RH of 33 % is slower than that at a RH of 97 %, and it is located between R4 and R3 in hcp at the RH of 97 %. Thus, the "universal" process R3 most likely becomes slower with drying at lower RH due to a stronger interaction with the pore surfaces. R1 is slower at a RH of 33 %, compared with 97 %, while R2 is more or less unaffected. Both R1 and R2 are probably due to local reorientations of water molecules which takes part of the structure in C-S-H, and therefore these dynamical processes are not substantially influenced by the total water content in the samples.

Relaxation process 4 (R4) is not detected in P145 at the RH of 33 %, which implies that this process is closely related to the moisture content. It was once assigned to the relaxation of water in large gel pores (3–12 nm) [35]. However, most of the water in these pores will crystallize to form ice and liquid water may exist only above the temperature of about −50 °C (see melting curve in Figs. 1 and 3). It is apparent that R4 is observed at the temperatures lower than the melting temperature and the relaxation strength remains almost constant at temperatures above the melting (see Fig. 8). Instead, it is more likely due to a Maxwell–Wagner process, which is related to interfacial polarization between bulk liquid and solid faces [75]. The broadening factor of a uniform Maxwell-Wagner process is 1. However, this process in hcp has
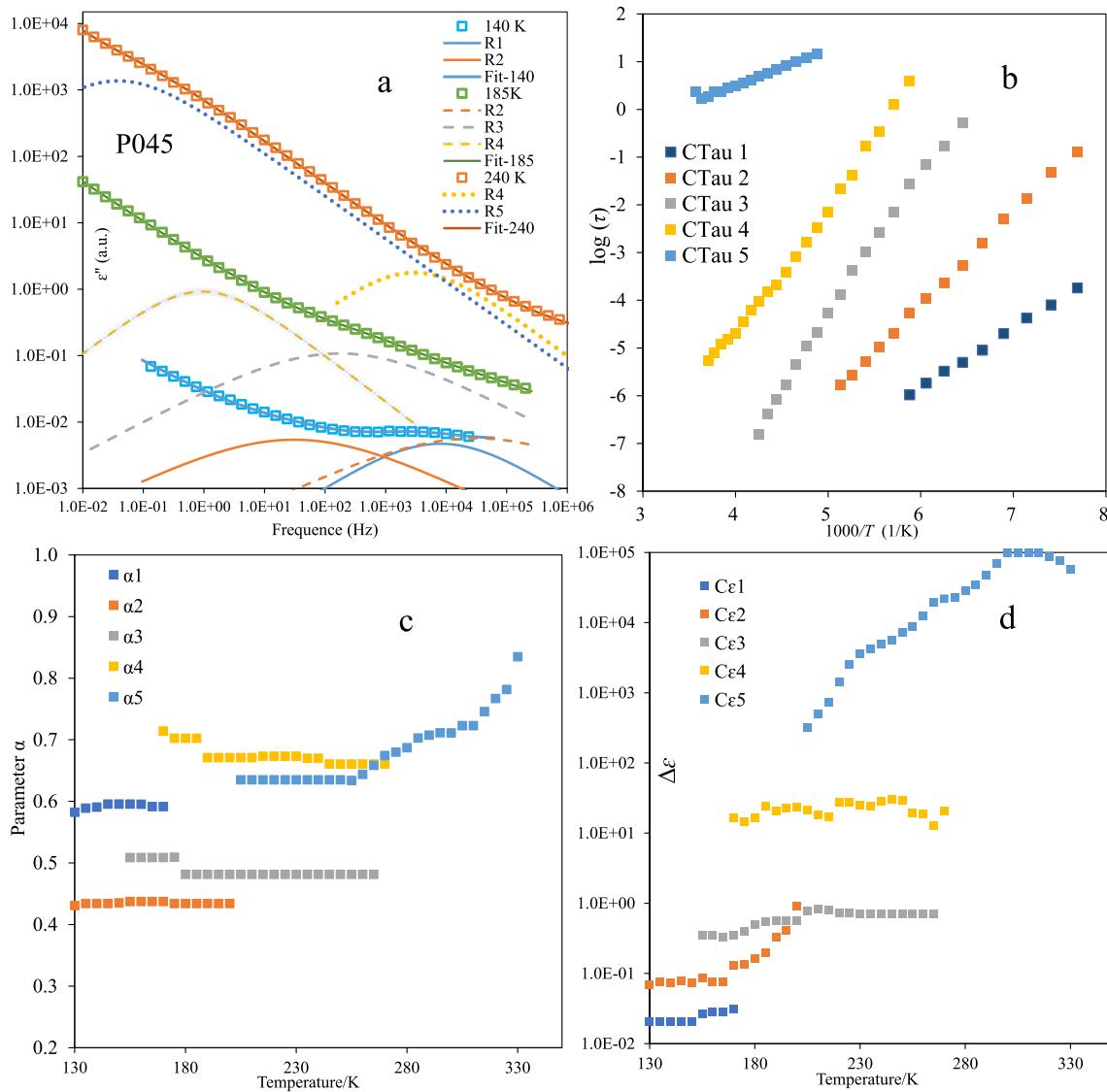
Fig. 8. Display of the general fitting of relaxation data of P045 with RH of 97 %: Graph a - Match between the fitted line and the measured results; Graph b - The generalized relaxation time at different temperatures; Graph c - Broadening parameter at different temperatures; Graph d - Strength of dielectric relaxation.

a broadening factor in range from 0.65 to 0.75, which implies a wide range of pore size distribution. The saddle-like temperature dependence of the relaxation time at higher temperatures ($1000/T$ in the range 3–4) is ascribed to the loss of evaporable water during heating. This somehow can explain why R4 is missing for samples at the RH of 33 %, since the drying of water in gel pores will decrease the interfacial area between bulk liquid and solid surface. Relaxation process 5 (R5) is the slowest process and it occurs in the dielectric spectrum at temperatures above the onset of melting obtained by LT-DSC. Furthermore, its relaxation strength is anomalously high (see Fig. 8 and figures in SI). A similar relaxation in clay materials was explained to be caused by the percolation of diffusing charge carriers in connected pores [73]. However, a further investigation is needed for better understanding this relaxation process, and it will not be further considered in this study since it is unlikely related to water dynamics.

The relaxation times of the different relaxation processes obviously depend on the temperature. Two common equations are used to describe the temperature dependence. The first one is the Arrhenius equation [81], and it is given by:

$$\tau = \tau_0 exp\left(\frac{E_a}{k_B T}\right) \tag{8}$$

where τ_0 is the pre-exponential time constant, E_a is the activation energy of the relaxation process, and k_B is Boltzmann constant. The Arrhenius temperature dependence is typical for more local and non-cooperative relaxation processes, often denoted as β-relaxations.

The second equation is called the Vogel-Fulcher-Tammann (VFT) equation [31,82], and it is given by:

$$\tau = \tau_0 exp\left(\frac{DT_0}{T - T_0}\right) \tag{9}$$

where D is a parameter related to the fragility (how much the temperature dependence deviates from an Arrhenius dependence), and T_0 is the temperature at which the dynamics of the system diverge to an infinitely slow relaxation time. The VFT temperature dependence is typically observed for cooperative relaxation processes as the viscosity related structural relaxation, commonly denoted as the α-relaxation.

Fig. 9 shows that the dynamics of structural water (R1 and R2) is a β-process with an Arrhenius dependence. The supercooled water confined in the gel pores seems to have a VFT dependence at relatively high temperatures. This fragile-to-strong crossover (from VFT to Arrhenius) is commonly occurring for supercooled water confined in a hydrophilic porous matrix [19,32]. R4 also has an Arrhenius
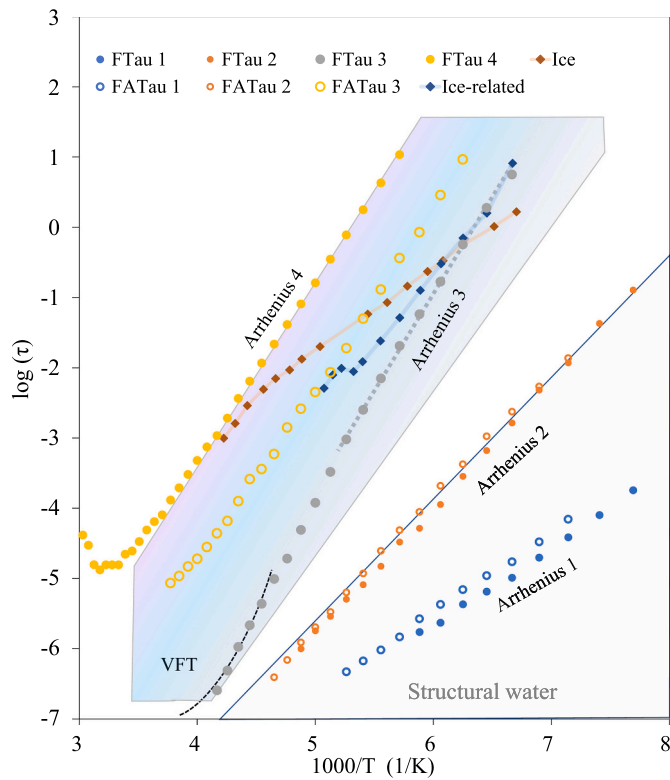
Fig. 9. Relaxation times of P145 at the RH of 97 % (FTau*) and 33 % (FATau*). Data of an ice relaxation is adopted from literature, ice l_h [79] and an ice-related relaxation in frozen tri-propylene glycol solution [80] are shown for comparison.

Table 3

Fitting parameters by using the Arrhenius equation to describe the temperature dependence of the water-related relaxation processes in hcps at the RH of 97 % and P145 at the RH of 33 %.

Mix ID	Relaxation	Slope (k)	Log(τ_0)	R^2	E_a (kJ/mol)
P045	R1	1.237	−13.25	0.998	23.67
	R2	1.946	−15.78	0.999	37.24
	R3	2.607	−17.02	0.996	49.90
	R4	2.896	−16.52	0.997	55.42
P145	R1	1.119	−12.39	0.998	21.41
	R2	1.818	−14.89	0.999	34.79
	R3	2.671	−16.97	0.998	51.11
	R4	2.500	−13.29	0.999	47.84
P245	R1	1.297	−13.63	0.997	24.82
	R2	1.836	−15.11	0.998	35.13
	R3	2.582	−16.91	0.996	49.41
	R4	2.870	−15.68	0.996	54.92
P345	R1	1.027	−11.85	0.998	19.65
	R2	1.944	−15.73	1	37.20
	R3	2.196	−14.50	0.994	42.02
	R4	2.831	−15.68	0.999	54.17
P145RH33	R1	1.146	−12.36	0.998	21.93
	R2	1.832	−14.85	0.999	35.06
	R3	2.484	−14.68	0.998	47.53

dependence in the temperature range below 250 K. All the fitting results for the relaxation processes with an Arrhenius behavior are presented in Table 3, which will be further discussed in next section.

3.5. Effect of SCMs on the water-related relaxation processes

Fig. 10 presents a comparison of the relaxation times of the water-related processes in hcps with different binder systems. Blending of 35 % SCMs has weak effects on the broadening parameter (see SI) and
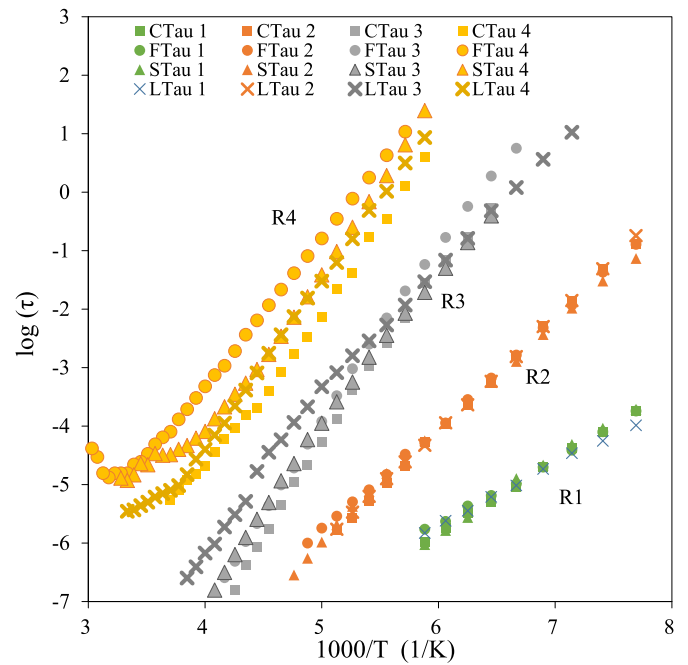

Fig. 10. Comparisons of the relaxation times of processes in hcps at the RH of 97 %, including CEM I paste (CTau*), the fly ash blended paste (FTau*), the slag binary pastes (STau*) and the ternary paste (LTau*).

the relaxation time of the structural water, but it changes the relaxation strength of R1 and R2. The blended hcps have a much higher relaxation strength than the CEM I paste for R1 (see Fig. S1). It is well recognized that the blending of slag and fly ash will reduce the Ca/Si ratio of C-S-H [83,84]. The structure of C-S-H with a lower Ca/Si ratio has a higher content of OH attached to the Si atoms [85]. Furthermore, both fly ash and slag will increase the amount of *Al* incorporated in the structure [86], which may increase the layer distance of the calcium aluminosilicate hydrate [87]. These dual effects induce a larger number of water molecules attached to the hydroxyl groups in silanol, thus resulting in the highest relaxation strength of R2 among the four binder systems below 160 K. Garcia-Lodeiro et al. [34] also reported that decalcification of C-S-H had almost no effects on the relaxation time of these two processes but changed the relaxation strength of each process. The fly ash blended paste dried at 33 % RH has a much lower relaxation strength than that samples dried at 97 % RH for both R2 and R1 (see Fig. S2 in SI), but their relaxation times are almost the same. This confirms that a change of the interlayer water content has minor effects on the dynamics (relaxation times) of R1 and R2.

The CEM I paste has the fastest R3 and R4 relaxations among the samples. A high concentration of Na^+ and OH^- will attract water around these ions to form a hydration shell, which weakens the hydrogen bonds of these water molecules and even decreases the average number of hydrogen bonds for the water molecules [88]. The concentration of alkali ions and the pH of the pore solution is determined by the composition of binders and the solubility of ions. For the binders used in this study, the CEM I paste has the highest concentration of alkali ions [89], so this may be the reason for the fastest water dynamics. The Maxwell–Wagner process, also called interfacial relaxation, originates from the existence of free charge carriers inside the system. These carriers migrate under the applied electrical field and accumulate at the interfaces in the system to induce polarization [90]. SCMs will modify the surface structure of pore wall for water adsorption [9] as well as the concentration of ions. Therefore, both the relaxation time and strength of R4 are altered by the blending of SCMs. Blending of SCMs will make R4 slower, and as shown in Fig. 10, this effect is most pronounced for fly ash. The relaxation strength of R3 is not necessarily determined by the
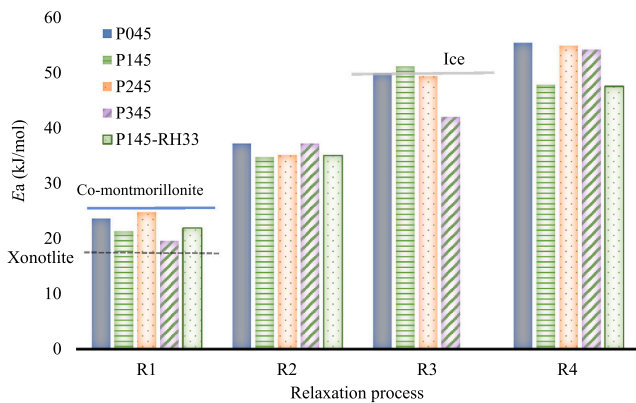
Fig. 11. Activation energies (E_a) of the different water-related relaxation processes in hcps.

Fig. 12. Heat capacity of P045 and P145 at the RH of 33 % compared to the heat capacity of concentrated aqueous solutions reported in published papers [95,96].

amount of water molecules in pores between 1 nm and 2.4 nm, because it is a result of the hydrogen bond relaxation [78,91], and therefore proportional to the total number of hydrogen bonds. This may explain why the CEM I paste has the lowest strength of R3 (see the SI), although it has the highest amount of unfrozen water (see Fig. 5).

Table 3 shows a comparison of fitting parameters obtained by using Arrhenius equation to describe the temperature dependence of the relaxation processes, and Fig. 11 presents a comparison of the regressed activation energies. The activation energy of R1 is in a range of 19.65–24.85 kJ/mol. Those values are higher than the activation energy of the Si-OH relaxation in xonotlite (17.28 kJ/mol or 0.18 ev) [36] but lower than the activation energy of the a similar relaxation found in Co-montmorillonite (25 kJ/mol) [73]. The addition of fly ash and limestone does not have any significant influence on the activation energy of R1, although there is a slight increase in $Log(\tau_0)$. Similarly, drying P145 at 33 % RH has little effect on the activation energy and $Log(\tau_0)$ of the structural water, compared with the paste conditioned at 97 % RH. The activation energy of R2 remains almost the same across all binder systems, ranging from 34.79 to 37.42 kJ/mol. The characteristics of R2 are quite similar to process 2 in the synthetic C-S-H [34] and tobermorite [36]. The activation energy of R3 is close to the activation energy of glassy bulk water, also called amorphous ice (45 kJ/mol [78]), but lower than the activation energy of the hexagonal crystal ice (ice l_h) (~ 50 kJ/mol [79,92]). Fly ash slightly increases the activation energy of R3, probably due to a lower ion concentration in the pore solution. The effect of slag on this process is mainly present at high temperatures, in the non-Arrhenius regime,so at lower temperatures P245 has a similar activation energy and $Log(\tau_0)$ as P045. Replacement of CEM I with 16 % limestone and 35 % slag reduces the activation energy. Fly ash causes a lower activation energy of R4 compared to the CEM I paste. Slag has minor effect on the activation energy of R4, but it increases $Log(\tau_0)$.

4. General discussion

4.1. Structure of the unfrozen water in interlayer and gel pores

The term "water" typically refers to a liquid phase; however, at temperatures below the glass transition temperature (which value is still debated, see in Ref. [78]), glassy water can exist. Despite being a solid, its structure displays a disordered arrangement similar to that of the liquid state [93], and as seen in this and other papers it also exhibits comprehensive local dynamics, as even crystalline ice phases do. Since bulk water instantaneously undergoes crystallization to ice below approximately 235 K, water in confined geometries has been employed as a model to reveal the structural and dynamical properties of bulk water in the deeply supercooled regime [19]. The potential correlation between supercooled confined water, glassy water, and amorphous bulk
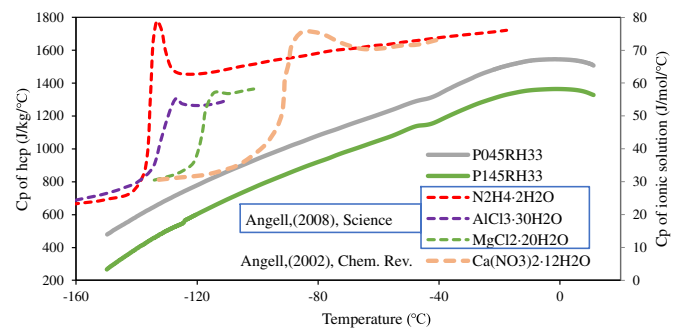
ice has been thoroughly discussed in various studies [32,78,94]. Fig. 12 illustrates the heat capacity of CEM I and fly ash paste during the cooling process from room temperature to −150 °C. There is no signal for any glass transition of unfrozen water in hcps at 33 % RH, in consistency with all types of confined water [94]. Only concentrated bulk aqueous solutions exhibit a glassy transition, resulting in a significant reduction of the heat capacity between −100 and − 145 °C, as shown in Fig. 12 for some solutions [95,96].

It has been discovered that unfrozen water in C-S-H exhibits reactivity. A substantial portion of the water present in the pore space of the C-S-H gel dissociates to form Ca-OH and Si-OH groups [97]. The hydroxyl groups present in these structures exhibit the fast R1 relaxation. Water in disconnected small pores shows an ice-like behavior, causing a hydraulic increase in the C-S-H shear strength.

The structure of water confined in C-S-H nanoslits with a size <~2.5 nm is largely affected by the hydrophilic surface. According to molecular dynamics simulations [98], the hydrophilicity of the C-S-H nanopore space is due to nonbridging oxygen atoms on disordered silicate chains. These serve as hydrogen-bond acceptors, directing hydrogen atoms of interfacial water molecules towards calcium-silicate layers. Water in this space has a distinct multirange structure: a distorted tetrahedral arrangement within 2.7 Å and a disordered arrangement resembling similar to dense fluids within 4.2 Å [98]. Such water structure results in the second fastest relaxation of water, R2. The activation energy of supercooled water confined in small gel pores indicates the dynamics of water clusters with a reduced number of hydrogen bonds [33]. According to modelling results the average number of hydrogen bonds in bulk water is approximately 3.6 per water molecule. However, for water molecules confined in C-S-H the average number of hydrogen bonds is typically as low as 2.34 [98].

The absence of a glass transition in confined water may be attributed to the limited volume, preventing cooperative rearrangements of water molecules into an ice-like tetrahedral network structure [94]. The suggested glassy structure of water in C-S-H layer [98] is expected to have the observed Arrhenius temperature-dependent dynamics at low temperatures, while the crossover to a VFT behavior at about 225 K (see Fig. 10) [33,99] suggests that the dynamics becomes more fluid-like and cooperative in character above that temperature.

4.2. Effect of SCMs on the water distribution and its dynamics

Blending of SCMs modifies the pore size distribution in hcps so the moisture capacity becomes different from CEM I pastes [2]. Among all of the binder systems, Blending of 35 % fly ash results in the highest moisture content among hcps at 97 % RH. The disparities are mainly observed for the liquid confined in large gel pores (a size range of approximately 4 nm to 8 nm). The binary paste with 35 % slag has a slightly smaller volume of water confined in the gel pores, but a larger volume of water in capillary pores (>8 nm) compared to the paste

blended with fly ash. In all pore size ranges, the CEM I paste exhibits the lowest ice formation. These results align with the outcomes of water vapour desorption [9]. When cement is partially replaced by 16 % limestone, the amount of freezable water decreases even further compared with the slag binary paste.

SCMs increase the amount of frozen water but reduce the amount of unfrozen water. Drying at 75 % RH shows no increase of water confined in small gel pores (<2.4 nm) in both CEM I and blended pastes. The main loss occurs in the volume of unfrozen water during the drying between 75 % and 50 % RH, which can mainly be attributed to coarsening of gel pores leading to a redistribution of water. The slag blended paste has the smallest reduction of unfrozen water, but it presents the largest increase in unfrozen water during a drying from 50 % to 33 % RH, which may be due to severer change of its unstable structure during the drying.

Three kinds of relaxation dynamics have been detected for the unfrozen water in hcps. The impact of 35 % fly ash, 35 % slag and 16 % limestone on the relaxation time of structural water is found to be very limited in this study. In addition, it is well acknowledged that blending of slag and fly ash modifies the structure of C-S-H [83,84], and reduces the Ca/Si ratio to increase the number of H atoms attached to the non-bridging oxygens [85]. Therefore, the blended pastes have a higher relaxation strength of R1 compared with CEM I pastes. Furthermore, fly ash largely elevates the quantity of the incorporated *Al* in the structure [86], potentially increasing the layer distance of calcium aluminosilicate hydrate [87]. These two effects result in the highest number of water molecules attached to the silanol group, thus causing the highest relaxation strength of R2 among the four binder systems below 160 K.

It has been observed that SCMs have a significant influence on the relaxation properties of water molecules in gel pores, changing the relaxation time and strength of R3. This can be attributed to the lower concentration of alkali ions in the pore solution of the blended pastes compared with CEM I, which attracts water molecules to form a hydration shell and thereby reducing the average number of hydrogen bonds between those and neighboring water molecules [88]. Furthermore, the blending of SCMs can also affect the surface feature of pores to modify absorption of water near the pore walls [9], leading to changes in the relaxation time and strength of R4. Therefore, it is important to consider the impact of SCMs on the relaxation properties of water molecules and its relation to the transport of ions when designing the blended cementitious materials.

4.3. Limitations

An exposure to low-temperature enforces effects on the microstructure of the layered materials [42] as well as the C-S-H [45]. Although Fig. 3 shows that only few irreversible effects were observed during the fast DSC scan procedure, an understanding of how the reversible change impacts the moisture distribution will determine the reliability in assessing the moisture distribution in hcps by the thermoporometry method. The use of Gibbs-Thomson equation may induce the deviation between the real size and calculated size of pores in the ultra-confined condition [100]. This study used thermoporometry to perform a comparative investigation between different binder systems. Therefore, it is worth noting that the discussion is partially based on the assumption that the influence of low temperatures on the microstructure is similar across mixes with different binders, and the deviations from Gibbs-Thomson equation are similar in different samples. A small amount of water is confined in some other layered phases in hydration products such as AF-phases and magnesium silicate hydrate. However, the mass percentage of these phases is <10 %, and SCMs have very limited effect on the amount of them [9]. It is an interesting problem for future investigation on how is the difference between dynamics of water confined in C-S-H and other layered phases. Excluding discussion of other layered phases will not affect conclusions for comparative study in this paper. One additional point to consider is that relaxation process R3 encompasses both the dynamics of unfrozen water and ice. It is

challenging to distinguish these two processes in the dielectric relaxation curve. A combination of other methods, such as quasi-elastic neutron scattering and NMR, may be helpful for a further investigation of the nature of the water dynamics [101].

5. Conclusions

Moisture in hardened cement-based paste would redistribute due to the dynamic microstructural change during the drying process. Blending of SCMs impacts the moisture redistribution and the dynamics of water confined in nanoscale pores to alter the performance of cement-based materials. The main findings in this study can be summarized as below.

During the fast low-temperature differential scanning calorimetry measurement, there are almost no irreversible changes of water distribution in the fly ash blended and ternary pastes. Thermoporometry works well in characterizing moisture distribution in cement-based materials at various RH levels. The melting curve is better than the freezing curve for the evaluation of water distribution in hcp. It enables to measure the water confined in pores larger than ~2.4 nm. No matter freezing down to any temperature, water in pores smaller than this critical size, including the interlayer and a part of gel pores, will not form a tetrahedral ice structure due to the limited number of hydrogen bonds. However, this part of water can be measured by a combination of the LT-DSC and the vacuum drying test.

SCMs influence not only the moisture distribution in hcp equilibrated at 97 % RH, but also the redistribution of water during a serial drying RH down to 33 %. It is confirmed that paste containing 35 % fly ash has the highest moisture content among all mixes, and its moisture loss during the drying at 75 % RH is the largest. The amount of unfrozen water in hcps is reduced by the blending of SCMs, but the slag blended pastes have a higher volume of freezable water compared with CEM I paste equilibrated at the same RH. The presence of limestone in ternary pastes enforces a reducing effect on the freezable water content potentially to improve the frost resistance of concretes.

A drying at 75 % RH lowers the content of the unfrozen water in both CEM I and the blended pastes compared with those at 97 % RH. This figures out some puzzles in the discussion of dynamical pore structure changes during the first drying between different publications [23,24,57]. This study confirms that the drying process has no increasing effect on volume of pores <2.7 nm, at least at the equilibrium conditions. An evident coarsening of gel pores may occur during the drying between 75 % and 55 % RH, which results in the phenomenon that the volume of unfrozen water has a considerable loss during this interval. A drying at 33 % RH causes an increase in the volume of unfrozen water due to the microstructural change of hydration products.

Five dynamical relaxation processes have been detected, and four of which are related to the water dynamics. The two fastest processes are dynamical behavior of the structural water in layered hydration products, corresponding the hydroxyl in Si-OH (R1) and water confined in the interlayer space (R2). Blending of SCMs with amount in this study have few effects on relaxation time of these two processes. The third fastest process (R3) is ascribed to the relaxation of water molecules with reduced hydrogen bonds and mixed with the ice relaxation. It will be altered by the SCMs, which probably is due to their dilution effect on ion concentration in the pore solution. The fourth process (R4) derives from the interfacial polarization between the bulk liquid and solid, and SCMs slow down this process. These results would update the understanding of change in C-S-H microstructure during the first drying process and the mechanism of how SCMs affect the water and ion transport in the nanosized channels.

CRediT authorship contribution statement

Liming Huang: Conceptualization, Methodology, Investigation, Data analysis, Writing-Original Draft, Writing-Review & Editing. Helén Jansson: Investigation, Writing-Review & Editing. Jan Swenson:

Investigation, Writing-Review & Editing, Project administration. Luping Tang: Writing-Review & Editing, Supervision, Project administration, Funding acquisition. Zhenghong Yang: Review & Editing, Supervision, Project administration.

Declaration of competing interest

We declare that there are no known competing financial interests or personal relationships that could have appeared to influence the work reported in this paper.

Data availability

Data will be made available on request.

Acknowledgements

Appendix A. Supplementary data

Supplementary data to this article can be found online at https://doi.org/10.1016/j.cemconres.2023.107333.

References

[1] V. Baroghel-Bouny, M. Thiéry, X. Wang, Modelling of isothermal coupled moisture–ion transport in cementitious materials, Cem. Concr. Res. 41 (2011) 828–841, https://doi.org/10.1016/j.cemconres.2011.04.001.

[2] L. Huang, L. Tang, I. Löfgren, N. Olsson, Z. Yang, Y. Li, Moisture and ion transport properties in blended pastes and their relation to the refined pore structure, Cem. Concr. Res. 161 (2022) 106949, https://doi.org/10.1016/j.cemconres.2022.106949.

[3] S. Ahmad, Reinforcement corrosion in concrete structures, its monitoring and service life prediction—a review, Cem. Concr. Compos. 25 (2003) 459–471.

[4] P.J. Prado, B.J. Balcom, S.D. Beyea, T.W. Bremner, R.L. Armstrong, P.E. Grattan-Bellew, Concrete freeze/thaw as studied by magnetic resonance imaging, Cem. Concr. Res. 28 (1998) 261–270, https://doi.org/10.1016/S0008-8846(97)00222-6.

[5] Z.P. Bazant, J.-C. Chern, A.M. Rosenberg, J.M. Gaidis, Mathematical model for freeze-thaw durability of concrete, J. Am. Ceram. Soc. 71 (1988) 776–783, https://doi.org/10.1111/j.1151-2916.1988.tb06413.x.

[6] F. Rajabipour, E. Giannini, C. Dunant, J.H. Ideker, M.D.A. Thomas, Alkali–silica reaction: current understanding of the reaction mechanisms and the knowledge gaps, Cem. Concr. Res. 76 (2015) 130–146, https://doi.org/10.1016/j.cemconres.2015.05.024.

[7] P.J.M. Monteiro, S.A. Miller, A. Horvath, Towards sustainable concrete, Nat. Mater. 16 (2017) 698–699, https://doi.org/10.1038/nmat4930.

[8] M. Schneider, The cement industry on the way to a low-carbon future, Cem. Concr. Res. 124 (2019) 105792, https://doi.org/10.1016/j.cemconres.2019.105792.

[9] L. Huang, L. Tang, L. Wadsö, I. Löfgren, N. Olsson, Z. Yang, Using water vapour and N2 isotherms to unveil effects of SCMs on nanopores and evaluate hydration degree, Cem. Concr. Res. 164 (2023) 107042, https://doi.org/10.1016/j.cemconres.2022.107042.

[10] R. Schmidt, E.W. Hansen, M. Stoecker, D. Akporiaye, O.H. Ellestad, Pore size determination of MCM-51 mesoporous materials by means of 1H NMR spectroscopy, N2 adsorption, and HREM. A preliminary study, J. Am. Chem. Soc. 117 (1995) 4049–4056, https://doi.org/10.1021/ja00119a021.

[11] A. Valori, P.J. McDonald, K.L. Scrivener, The morphology of C–S–H: lessons from 1H nuclear magnetic resonance relaxometry, Cem. Concr. Res. 49 (2013) 65–81, https://doi.org/10.1016/j.cemconres.2013.03.011.

[12] C. Zhou, F. Ren, Q. Zeng, L. Xiao, W. Wang, Pore-size resolved water vapor adsorption kinetics of white cement mortars as viewed from proton NMR relaxation, Cem. Concr. Res. 105 (2018) 31–43, https://doi.org/10.1016/j.cemconres.2017.12.002.

[13] A.C.A. Muller, K.L. Scrivener, A.M. Gajewicz, P.J. McDonald, Use of bench-top NMR to measure the density, composition and desorption isotherm of C–S–H in

[14] I. Foley, S.A. Farooqui, R.L. Kleinberg, Effect of paramagnetic ions on NMR relaxation of fluids at solid surfaces, J. Magn. Reson. Ser. A 123 (1996) 95–104, https://doi.org/10.1006/jmra.1996.0218.

[15] M. Brun, A. Lallemand, J.-F. Quinson, C. Eyraud, A new method for the simultaneous determination of the size and shape of pores: the thermoporometry, Thermochim. Acta 21 (1977) 59–88.

[16] S. Irico, D. Gastaldi, F. Canonico, G. Magnacca, Investigation of the microstructural evolution of calcium sulfoaluminate cements by thermoporometry, Cem. Concr. Res. 53 (2013) 239–247, https://doi.org/10.1016/j.cemconres.2013.06.012.

[17] S.W. Tang, Z. He, X.H. Cai, R.J. Cai, W. Zhou, Z.J. Li, H.Y. Shao, T. Wu, E. Chen, Volume and surface fractal dimensions of pore structure by NAD and LT-DSC in calcium sulfoaluminate cement pastes, Constr. Build. Mater. 143 (2017) 395–418, https://doi.org/10.1016/j.conbuildmat.2017.03.140.

[18] Z. Sun, G.W. Scherer, Pore size and shape in mortar by thermoporometry, Cem. Concr. Res. 40 (2010) 740–751, https://doi.org/10.1016/j.cemconres.2009.11.011.

[19] S. Cerveny, F. Mallamace, J. Swenson, M. Vogel, L. Xu, Confined water as model of supercooled water, Chem. Rev. 18 (2016).

[20] A.C.A. Muller, K.L. Scrivener, A.M. Gajewicz, P.J. McDonald, Densification of C–S–H measured by ^{1}H NMR Relaxometry, J. Phys. Chem. C 117 (2013) 403–412, https://doi.org/10.1021/jp3102964.

[21] H.M. Jennings, A. Kumar, G. Sant, Quantitative discrimination of the nano-pore-structure of cement paste during drying: new insights from water sorption isotherms, Cem. Concr. Res. 76 (2015) 27–36, https://doi.org/10.1016/j.cemconres.2015.05.006.

[22] J. Yin, W. Li, J. Wang, X. Kong, Irreversible microstructural changes of calcium silicate hydrate during the first drying-resaturation cycle, Cem. Concr. Res. 163 (2023) 107032, https://doi.org/10.1016/j.cemconres.2022.107032.

[23] C. Zhou, X. Zhang, Z. Wang, A discussion of the paper "Dynamic microstructural evolution of hardened cement paste during first drying monitored by 1H NMR relaxometry" by I. Maruyama, T. Ohkubo, T. Haji et al. Cem. Concr. Res. 128 (2020), 105928 https://doi.org/10.1016/j.cemconres.2019.105928.

[24] I. Maruyama, T. Ohkubo, T. Haji, R. Kurihara, Reply to Zhou et al.'s "A discussion of the paper 'Dynamic microstructural evaluation of hardened cement paste during first drying monitored by 1H NMR relaxometry'", Cem. Concr. Res. 137 (2020), 106219 https://doi.org/10.1016/j.cemconres.2020.106219.

[25] T.C. Powers, T.L. Brownyard, Studies of the Physical Properties of Hardened Portland Cement Paste, 1946, pp. 101–132.

[26] H.M. Jennings, A model for the microstructure of calcium silicate hydrate in cement paste, Cem. Concr. Res. 30 (2000) 101–116, https://doi.org/10.1016/S0008-8846(99)00209-4.

[27] H.M. Jennings, Refinements to colloid model of C-S-H in cement: CM-II, Cem. Concr. Res. 38 (2008) 275–289, https://doi.org/10.1016/j.cemconres.2007.10.006.

[28] P.J. McDonald, V. Rodin, A. Valori, Characterisation of intra- and inter-C–S–H gel pore water in white cement based on an analysis of NMR signal amplitudes as a function of water content, Cem. Concr. Res. 40 (2010) 1656–1663, https://doi.org/10.1016/j.cemconres.2010.08.003.

[29] T.C. Powers, The air requirement of frost-resistant concrete, in: Highway Research Board 33, PCA Bulletin, 1949, pp. 184–211.

[30] O. Coussy, P.J.M. Monteiro, Poroelastic model for concrete exposed to freezing temperatures, Cem. Concr. Res. 38 (2008) 40–48, https://doi.org/10.1016/j.cemconres.2007.06.006.

[31] R. Bergman, J. Swenson, Dynamics of supercooled water in confined geometry, Nature. 403 (2000) 283–286.

[32] J. Swenson, Possible relations between supercooled and glassy confined water and amorphous bulk ice, Phys. Chem. Chem. Phys. 20 (2018) 30095–30103, https://doi.org/10.1039/C8CP05688A.

[33] S. Cerveny, S. Arrese-Igor, J.S. Dolado, J.J. Gaitero, A. Alegría, J. Colmenero, Effect of hydration on the dielectric properties of C-S-H gel, J. Chem. Phys. 134 (2011), 034509, https://doi.org/10.1063/1.3521481.

[34] I. Garcia-Lodeiro, G. Goracci, J.S. Dolado, M.T. Blanco-Varela, Mineralogical and microstructural alterations in a portland cement paste after an accelerated decalcification process, Cem. Concr. Res. 140 (2021) 106312, https://doi.org/10.1016/j.cemconres.2020.106312.

[35] G. Goracci, M. Monasterio, H. Jansson, S. Cerveny, Dynamics of nano-confined water in Portland cement - comparison with synthetic C-S-H gel and other silicate materials, Sci. Rep. 7 (2017) 8258, https://doi.org/10.1038/s41598-017-08645-z.

[36] V. Musumeci, G. Goracci, P. Sanz Camacho, J.S. Dolado, C. Aymonier, Correlation between the dynamics of nanoconfined water and the local chemical environment in calcium silicate hydrate nanominerals, Chem. Eur. J. 27 (2021) 11309–11318, https://doi.org/10.1002/chem.202100098.

[37] L. Greenspan, Humidity fixed points of binary saturated aqueous solutions, J. Res. Natl. Bur. Stan. Sect. A. 81A (1977) 89, https://doi.org/10.6028/jres.081A.011.

[38] C. Alba-Simionesco, B. Coasne, G. Dosseh, G. Dudziak, K.E. Gubbins, R. Radhakrishnan, M. Sliwinska-Bartkowiak, Effects of confinement on freezing and melting, J. Phys. Condens. Matter 18 (2006) R15–R68, https://doi.org/10.1088/0953-8984/18/6/R01.

[39] H. Kanda, M. Miyahara, K. Higashitani, Solidification of Lennard-Jones fluid in cylindrical nanopores and its geometrical hindrance effect: a Monte Carlo study, Langmuir 16 (2000) 8529–8535, https://doi.org/10.1021/la991659p.

[40] D.H. Bager, E.J. Sellevold, Ice formation in hardened cement paste, part I — room temperature cured pastes with variable moisture contents, Cem. Concr. Res. 16 (1986) 709–720, https://doi.org/10.1016/0008-8846(86)90045-1.

[41] K. Kurumisawa, O.M. Jensen, Thermoporometry and proton NMR measurement on cement paste equilibrated at different relative humidities, ACT. 18 (2020) 456–462, https://doi.org/10.3151/jact.18.456.

[42] P.D. Svensson, S. Hansen, Freezing and thawing of montmorillonite — a time-resolved synchrotron X-ray diffraction study, Appl. Clay Sci. 49 (2010) 127–134, https://doi.org/10.1016/j.clay.2010.04.015.

[43] S. Jähnert, F. Vaca Chávez, G.E. Schaumann, A. Schreiber, M. Schönhoff, G. H. Findenegg, Melting and freezing of water in cylindrical silica nanopores, Phys. Chem. Chem. Phys. 10 (2008) 6039, https://doi.org/10.1039/b809438c.

[44] E.B. Moore, E. de la Llave, K. Welke, D.A. Scherlis, V. Molinero, Freezing, melting and structure of ice in a hydrophilic nanopore, Phys. Chem. Chem. Phys. 12 (2010) 4124, https://doi.org/10.1039/b919724a.

[45] X. Zhu, C. Qian, B. He, Q. Chen, Z. Jiang, Experimental study on the stability of C-S-H nanostructures with varying bulk CaO/SiO_2 ratios under cryogenic attack, Cem. Concr. Res. 135 (2020) 106114, https://doi.org/10.1016/j. cemconres.2020.106114.

[46] G. Geng, R.J. Myers, J. Li, R. Maboudian, C. Carraro, D.A. Shapiro, P.J. M. Monteiro, Aluminum-induced dreierketten chain cross-links increase the mechanical properties of nanocrystalline calcium aluminosilicate hydrate, Sci. Rep. 7 (2017) 44032, https://doi.org/10.1038/srep44032.

[47] B. Lothenbach, K. Scrivener, R.D. Hooton, Supplementary cementitious materials, Cem. Concr. Res. 41 (2011) 1244–1256, https://doi.org/10.1016/j. cemconres.2010.12.001.

[48] R. Wang, Z. Hu, Y. Li, K. Wang, H. Zhang, Review on the deterioration and approaches to enhance the durability of concrete in the freeze–thaw environment, Constr. Build. Mater. 321 (2022) 126371, https://doi.org/10.1016/j. conbuildmat.2022.126371.

[49] K. Bharadwaj, D. Glosser, M.K. Moradllo, O.B. Isgor, W.J. Weiss, Toward the prediction of pore volumes and freeze-thaw performance of concrete using thermodynamic modelling, Cem. Concr. Res. 124 (2019) 105820, https://doi. org/10.1016/j.cemconres.2019.105820.

[50] I. Maruyama, H. Sugimoto, S. Umeki, R. Kurihara, Effect of fineness of cement on drying shrinkage, Cem. Concr. Res. 161 (2022) 106961, https://doi.org/ 10.1016/j.cemconres.2022.106961.

[51] N. Bouzoubaâ, M.H. Zhang, V.M. Malhotra, Mechanical properties and durability of concrete made with high-volume fly ash blended cements using a coarse fly ash, Cem. Concr. Res. 31 (2001) 1393–1402, https://doi.org/10.1016/S0008-8846(01)00592-0.

[52] A. Aghaeipour, M. Madhkhan, Effect of ground granulated blast furnace slag (GGBFS) on RCCP durability, Constr. Build. Mater. 141 (2017) 533–541, https:// doi.org/10.1016/j.conbuildmat.2017.03.019.

[53] P. Duan, Z. Shui, W. Chen, C. Shen, Enhancing microstructure and durability of concrete from ground granulated blast furnace slag and metakaolin as cement replacement materials, J. Mater. Res. Technol. 2 (2013) 52–59, https://doi.org/ 10.1016/j.jmrt.2013.03.010.

[54] N. Olsson, L.-O. Nilsson, M. Åhs, V. Baroghel-Bouny, Moisture transport and sorption in cement based materials containing slag or silica fume, Cem. Concr. Res. 106 (2018) 23–32.

[55] C. Zhou, F. Ren, Q. Zeng, L. Xiao, W. Wang, Pore-size resolved water vapor adsorption kinetics of white cement mortars as viewed from proton NMR relaxation, Cem. Concr. Res. 105 (2018) 31–43, https://doi.org/10.1016/j. cemconres.2017.12.002.

[56] C. Zhou, X. Zhang, Z. Wang, Z. Yang, Water sensitivity of cement-based materials, J. Am. Ceram. Soc. 104 (2021) 4279–4296.

[57] I. Maruyama, T. Ohkubo, T. Haji, R. Kurihara, Dynamic microstructural evolution of hardened cement paste during first drying monitored by 1H NMR relaxometry, Cem. Concr. Res. 122 (2019) 107–117, https://doi.org/10.1016/j. cemconres.2019.04.017.

[58] D.W. Hwang, C.-C. Chu, A.K. Sinha, L.-P. Hwang, Dynamics of supercooled water in various mesopore sizes, J. Chem. Phys. 126 (2007) 044702, https://doi.org/ 10.1063/1.2429065.

[59] I.O. Yaman, N. Hearn, H.M. Aktan, Active and non-active porosity in concrete part I: experimental evidence, Mater. Struct. 35 (2002) 102–109, https://doi.org/ 10.1007/BF02482109.

[60] C. Roosz, S. Gaboreau, S. Grangeon, D. Prêt, V. Montouillout, N. Maubec, S. Ory, P. Blanc, P. Vieillard, P. Henocq, Distribution of water in synthetic calcium silicate hydrates, Langmuir. 32 (2016) 6794–6805, https://doi.org/10.1021/acs. langmuir.6b00878.

[61] P. Bayliss, Further interlayer desorption studies of CSH(1), Cem. Concr. Res. 3 (1973) 185–188, https://doi.org/10.1016/0008-8846(73)90046-X.

[62] C. Zhou, F. Ren, Q. Zeng, L. Xiao, W. Wang, Pore-size resolved water vapor adsorption kinetics of white cement mortars as viewed from proton NMR relaxation, Cem. Concr. Res. 105 (2018) 31–43, https://doi.org/10.1016/j. cemconres.2017.12.002.

[63] H.M. Jennings, A. Kumar, G. Sant, Quantitative discrimination of the nano-pore-structure of cement paste during drying: new insights from water sorption isotherms, Cem. Concr. Res. 76 (2015) 27–36, https://doi.org/10.1016/j. cemconres.2015.05.006.

[64] R.A. Helmuth, D.H. Turk, The Reversible and Irreversible Drying Shrinkage of Hardened Portland Cement and Tricalcium Silicate Pastes, Portland Cement Assoc r & d Lab Bull, 1967.

[65] A. Bentur, L.R. Berger, V.F. Lawrence Jr., Creep and drying shrinkage of calcium silicate pastes III. A hypothesis of irreversible strains, Cem. Concr. Res. 8 (1979) 721–732.

[66] I. Maruyama, N. Sakamoto, K. Matsui, G. Igarashi, Microstructural changes in white Portland cement paste under the first drying process evaluated by WAXS, SAXS, and USAXS, Cem. Concr. Res. 91 (2017) 24–32, https://doi.org/10.1016/j. cemconres.2016.10.002.

[67] L. Fumagalli, A. Esfandiar, R. Fabregas, S. Hu, P. Ares, A. Janardanan, Q. Yang, B. Radha, T. Taniguchi, K. Watanabe, G. Gomila, K.S. Novoselov, A.K. Geim, Anomalously low dielectric constant of confined water, Science. 360 (2018) 1339–1342, https://doi.org/10.1126/science.aat4191.

[68] M.H. Motevaselian, N.R. Aluru, Universal reduction in dielectric response of confined fluids, ACS Nano 14 (2020) 12761–12770, https://doi.org/10.1021/ acsnano.0c03173.

[69] N. Dilissen, J. Vleugels, J. Vermeiren, B. García-Baños, J.R.S. Marín, J.M. Catalá-Civera, Temperature dependency of the dielectric properties of hydrated and ordinary Portland cement and their constituent phases at 2.45 GHz up to 1100 °C, Cem. Concr. Res. 165 (2023), 107067, https://doi.org/10.1016/j. cemconres.2022.107067.

[70] S. Ait Hamadouche, T. Honorio, T. Bore, F. Benboudjema, F. Daout, E. Vourc'h, Dielectric permittivity of C-S-H, Cem. Concr. Res. 169 (2023) 107178, https:// doi.org/10.1016/j.cemconres.2023.107178.

[71] K.S. Cole, R.H. Cole, Dispersion and absorption in dielectrics I. Alternating current characteristics, J. Chem. Phys. 9 (1941) 341–351, https://doi.org/ 10.1063/1.1750906.

[72] M. Monasterio, H. Jansson, J.J. Gaitero, J.S. Dolado, S. Cerveny, Cause of the fragile-to-strong transition observed in water confined in C-S-H gel, J. Chem. Phys. 139 (2013) 164714, https://doi.org/10.1063/1.4826638.

[73] M.A. Vasilyeva, Y.A. Gusev, V.G. Shtyrlin, A. Greenbaum (Gutina), A. Puzenko, P. B. Ishai, Y. Feldman, Dielectric relaxation of water in clay minerals, Clay Clay Miner. 62 (2014) 62–73, https://doi.org/10.1346/CCMN.2014.0620106.

[74] L. Frunza, H. Kosslick, I. Pitsch, S. Frunza, A. Schönhals, Rotational fluctuations of water inside the nanopores of SBA-type molecular sieves, J. Phys. Chem. B 109 (2005) 9154–9159, https://doi.org/10.1021/jp044503t.

[75] J. Sjöström, J. Swenson, R. Bergman, S. Kittaka, Investigating hydration dependence of dynamics of confined water: monolayer, hydration water and Maxwell–Wagner processes, J. Chem. Phys. 128 (2008) 154503, https://doi.org/ 10.1063/1.2902283.

[76] S. Cerveny, G.A. Schwartz, J. Otegui, J. Colmenero, J. Loichen, S. Westermann, Dielectric study of hydration water in silica nanoparticles, J. Phys. Chem. C 116 (2012) 24340–24349, https://doi.org/10.1021/jp307826s.

[77] K. Amann-Winkel, C. Gainaru, P.H. Handle, M. Seidl, H. Nelson, R. Böhmer, T. Loerting, Water's second glass transition, Proc. Natl. Acad. Sci. U. S. A. 110 (2013) 17720–17725, https://doi.org/10.1073/pnas.1311718110.

[78] J. Swenson, J. Teixeira, The glass transition and relaxation behavior of bulk water and a possible relation to confined water, J. Chem. Phys. 132 (2010), 014508, https://doi.org/10.1063/1.3285286.

[79] S. Kawada, Dielectric anisotropy in ice Ih, J. Phys. Soc. Jpn. 44 (1978) 1881–1886.

[80] J.H. Melillo, J. Swenson, S. Cerveny, Influence of ice formation on the dynamic and thermodynamic properties of aqueous solutions, J. Mol. Liq. 356 (2022) 119039, https://doi.org/10.1016/j.molliq.2022.119039.

[81] F. Kremer, A. Schönhals (Eds.), Broadband Dielectric Spectroscopy, Springer Berlin Heidelberg, Berlin, Heidelberg, 2003, https://doi.org/10.1007/978-3-642-56120-7.

[82] J. Rault, Origin of the Vogel-Fulcher-Tammann Law in Glass-forming Materials: The α-β Bifurcation, 2000.

[83] B. Lothenbach, K. Scrivener, R.D. Hooton, Supplementary cementitious materials, Cem. Concr. Res. 41 (2011) 1244–1256, https://doi.org/10.1016/j. cemconres.2010.12.001.

[84] J. Skibsted, R. Snellings, Reactivity of supplementary cementitious materials (SCMs) in cement blends, Cem. Concr. Res. 124 (2019) 105799, https://doi.org/ 10.1016/j.cemconres.2019.105799.

[85] I.G. Richardson, Tobermorite/jennite- and tobermorite/calcium hydroxide-based models for the structure of C-S-H: applicability to hardened pastes of tricalcium silicate, β-dicalcium silicate, Portland cement, and blends of Portland cement with blast-furnace slag, metakaolin, or silica fume, Cem. Concr. Res. 34 (2004) 1733–1777, https://doi.org/10.1016/j.cemconres.2004.05.034.

[86] Z. Giergiczny, Fly ash and slag, Cem. Concr. Res. 124 (2019) 105826, https://doi. org/10.1016/j.cemconres.2019.105826.

[87] E. L'Hôpital, B. Lothenbach, G. Le Saout, D. Kulik, K. Scrivener, Incorporation of aluminium in calcium-silicate-hydrates, Cem. Concr. Res. 75 (2015) 91–103, https://doi.org/10.1016/j.cemconres.2015.04.007.

[88] A. Botti, F. Bruni, S. Imberti, M.A. Ricci, A.K. Soper, Ions in water: the microscopic structure of concentrated NaOH solutions, J. Chem. Phys. 120 (2004) 10154–10162, https://doi.org/10.1063/1.1705572.

[89] L. Huang, L. Tang, I. Löfgren, N. Olsson, Z. Yang, Real-time monitoring the electrical properties of pastes to map the hydration induced microstructure change in cement-based materials, Cem. Concr. Compos. 132 (2022) 104639, https://doi.org/10.1016/j.cemconcomp.2022.104639.

[90] G.C. Psarras, E. Manolakaki, G.M. Tsangaris, Dielectric dispersion and ac conductivity in—iron particles loaded—polymer composites, Compos. A: Appl. Sci. Manuf. 34 (2003) 1187–1198, https://doi.org/10.1016/j. compositesa.2003.08.002.

[91] J. Teixeira, A. Luzar, S. Longeville, Dynamics of hydrogen bonds: how to probe their role in the unusual properties of liquid water, J. Phys. Condens. Matter 18 (2006) S2353–S2362, https://doi.org/10.1088/0953-8984/18/36/S09.

[92] G.P. Johari, S.J. Jones, Dielectric properties of polycrystalline D2O ice Ih (hexagonal), Proc. R. Soc. Lond. A 349 (1976) 467–495.

[93] O. Mishima, H.E. Stanley, The relationship between liquid, supercooled and glassy water, Nature. 396 (1998) 329–335, https://doi.org/10.1038/24540.

[94] J. Swenson, K. Elamin, H. Jansson, S. Kittaka, Why is there no clear glass transition of confined water? Chem. Phys. 424 (2013) 20–25, https://doi.org/10.1016/j.chemphys.2012.11.014.

[95] C.A. Angell, Insights into phases of liquid water from study of its unusual glass-forming properties, Science. 319 (2008) 582–587, https://doi.org/10.1126/science.1131939.

[96] C.A. Angell, Liquid fragility and the glass transition in water and aqueous solutions, Chem. Rev. 102 (2002) 2627–2650, https://doi.org/10.1021/cr000689q.

[97] H. Manzano, S. Moeini, F. Marinelli, A.C.T. van Duin, F.-J. Ulm, R.J.-M. Pellenq, Confined water dissociation in microporous defective silicates: mechanism, dipole distribution, and impact on substrate properties, J. Am. Chem. Soc. 134 (2012) 2208–2215, https://doi.org/10.1021/ja209152n.

[98] M. Youssef, R.J.-M. Pellenq, B. Yildiz, Glassy nature of water in an Ultraconfining disordered material: the case of calcium−silicate−hydrate, J. Am. Chem. Soc. 133 (2011) 2499–2510, https://doi.org/10.1021/ja107003a.

[99] M. Monasterio, H. Jansson, J.J. Gaitero, J.S. Dolado, S. Cerveny, Cause of the fragile-to-strong transition observed in water confined in C-S-H gel, J. Chem. Phys. 139 (2013) 164714, https://doi.org/10.1063/1.4826638.

[100] L. Scalfi, B. Coasne, B. Rotenberg, On the Gibbs-Thomson equation for the crystallization of confined fluids, J. Chem. Phys. 154 (2021) 114711.

[101] T. Takamuku, M. Yamagami, H. Wakita, Y. Masuda, T. Yamaguchi, Thermal property, structure, and dynamics of supercooled water in porous silica by calorimetry, neutron scattering, and NMR relaxation, J. Phys. Chem. B 101 (1997) 5730–5739.